


ORIGINAL ARTICLE

Open Access



Thermal-Mechanical Effect and Removal Mechanism of Ti-6Al-4V During Laser-Assisted Grinding

Guijian Xiao^{1*} , Shengwang Zhu¹, Yi He¹, Gang Liu¹ and Yuanhe Ni¹

Abstract

The low density and high corrosion resistance of titanium alloy make it a material with various applications in the aerospace industry. However, because of its high specific strength and poor thermal conductivity, there are problems such as high cutting force, poor surface integrity, and high cutting temperature during conventional machining. As an advanced processing method with high efficiency and low damage, laser-assisted machining can improve the machinability of titanium alloy. In this study, a picosecond pulse laser-assisted scratching (PPLAS) method considering both the temperature-dependent material properties and ultrashort pulse laser's characteristics is first proposed. Then, the effects of laser power, scratching depth, and scratching speed on the distribution of stress and temperature field are investigated by simulation. Next, PPLAS experiments are conducted to verify the correctness of the simulation and reveal the removal behavior at various combinations of laser power and scratching depths. Finally, combined with simulated and experimental results, the removal mechanism under the two machining methods is illustrated. Compared with conventional scratching (CS), the tangential grinding force is reduced by more than 60% and the material removal degree is up to 0.948 during PPLAS, while the material removal is still primarily in the form of plastic removal. Grinding debris in CS takes the form of stacked flakes with a "fish scale" surface, whereas it takes the form of broken serrations in PPLAS. This research can provide important guidance for titanium alloy grinding with high surface quality and low surface damage.

Keywords Laser-assisted machining, Titanium alloy, Material removal, Thermal-mechanical effect, Finite element analysis

1 Introduction

As an engineering material, titanium alloy is widely used in the fan blades, impellers, blisks, and other core components of aero-engines because of its excellent characteristics such as low density, high strength, high heat resistance, and strong corrosion resistance [1, 2]. The Ti-6Al-4V (TC4) alloy stands out among them because it has strong all-around characteristics and there is a

body-centered cubic lattice β phase close to the α phase, which boosts the alloy's flexibility and fracture toughness, and can be used for a variety of machining [3, 4]. However, because of its poor thermal conductivity, low volume-specific heat, and thermal softening performance at high temperatures of TC4 [5], there are problems such as high temperature, severe tool wear, and high cutting force during processing [6, 7]. For this reason, the use of new machining methods can benefit the industrial application of this alloy.

As one of the most well-known heat-assisted machining methods, laser-assisted machining (LAM) involves the reduction of strength and thermal softening of locally heated materials through the high instantaneous heating

*Correspondence:

Guijian Xiao
xiaoguijian@cqu.edu.cn

¹ College of Mechanical and Vehicle Engineering, Chongqing University, Chongqing 400044, China

capacity of the laser [8, 9], which has many advantages, such as reduced specific energy [10–12], reduced tool wear [13, 14], and reduced roughness of the machined surface [15, 16]. Some researchers have conducted experiments to evaluate the advantages of titanium alloys during LAM. Ayed et al. [17] conducted experiments on laser-assisted cutting of TC4 alloy at different feeding speeds and cutting speeds, discovering that the cutting force could be reduced by 55% at most under different process parameters. By contrasting the machinability performance of TC4 alloy between conventional cutting and laser-assisted cutting, Dandekar et al. [18] found that the specific cutting energy under laser-assisted cutting was reduced, the surface roughness was improved, and the tool life was improved by a maximum of 1.7 times. At the same time, Xia et al. [19] positively evaluated laser-assisted micro milling of TC4 alloy in terms of cutting force, machined surface quality, burr formation, and tool wear. Tadavani et al. [20] conducted experiments on pulse laser-assisted cutting of Inconel 718 alloy under different laser parameters and discovered that the specific cutting energy was reduced by 35% at most, while the surface roughness was increased by 22% at most. According to a thorough evaluation of the surface integrity index of TC4 alloy under conventional machining and LAM by Kalantari et al. [3], LAM could greatly enhance the surface integrity of TC4 alloy under controlled process conditions. However, there is a lack of information on the detailed deformation behavior of TC4 alloy during LAM, especially the evolution mechanism of material removal during processing.

With the development of computational capacity, numerical analysis and finite element simulations are frequently used to predict the evolution of material removal in LAM. Germain et al. [21] created a time-dependent moving heat flux on the top surface of the workpiece using a Fortran subroutine, explaining the reduction of cutting force through changes in the temperature field and residual stress field during LAM. On this basis, Yang et al. [22] predicted the depth and width of the heat-affected zone of TC4 alloy by the moving Gaussian heat source method, and discovered that the trend was positively correlated with the laser power and negatively correlated with the spot diameter and scanning speed. You et al. [9] considered both cumulative thermal effects and thermal boundary conditions during laser processing, and discovered that surface finish quality was enhanced and tool wear was reduced during thermal laser-assisted cutting. Xi et al. [23] adopted the Johnson-Cook (J-C) model and the Zerilli-Armstrong model to simulate the LAM of titanium alloys, and found that the prediction results of the cutting force from the J-C model were in better agreement with the experimental results. Khatir

et al. [24] used the VDFLUX subroutine to forecast heat-affected zones, surface hardness changes, and white layer formation during laser-assisted cutting. It can be found that the current research by scholars mainly focuses on the continuous LAM of titanium alloys, with less research on pulsed LAM of titanium alloys, which limits the full utilization of thermal effects from the pulsed laser.

Due to its high hardness, strong wear resistance, outstanding thermochemical stability, and good self-sharpening qualities, cubic boron nitride (CBN) is getting popularity for grinding TC4 alloy [25, 26]. However, the anisotropic crystal structure of CBN abrasive grains can lead to macroscopic fracture and pull-out when subjected to high-impact forces during the grinding process [27]. Therefore, it is crucial to improve the material's machinability and reduce grinding force for increasing grinding efficiency and lowering tool damage while grinding TC4 alloy with CBN abrasive grain. In this study, a PPLAS method considering both the temperature-dependent material properties and the ultrashort pulse laser's characteristics is proposed. The force and temperature variations during CS and PPLAS are then studied. To comprehensively investigate the grinding force and material removal behavior under the two processing methods, comparative experiments are also conducted. The removal process of TC4 alloy during CS and PPLAS is finally revealed by combining simulated and experimental results, providing vital direction for high surface quality and low surface damage grinding of titanium alloy.

2 Simulation of Thermal-mechanical Coupling Moving PPLAS

The distinctiveness of the proposed method is that the stress field and temperature field distribution under different process parameter combinations are calculated, taking into account the characteristics of the pulsed laser and the dynamic properties of TC4 with temperature changes, thereby clarifying the material removal behavior. Material properties and the pulsed laser heat source functions are elaborated in Section 2.1. The removal behavior under different process parameter combinations is next investigated by simulation in Section 2.2, which provides a foundation for the selection of parameters for further PPLAS experiments.

2.1 Materials and Laser Heating Models

TC4 alloy is a medium-strength α - β type two-phase titanium alloy, and its main chemical compositions and physical properties are presented in Tables 1 [29] and 2 [30]. Eq. (1) [28] is used to characterize the dynamic mechanical characteristics of the material as simulated by the grinding process using the J-C viscoplastic intrinsic model.

Table 1 Chemical compositions of TC4 [29]

Element	Ti	Al	V	Fe	N+O
Content (%)	Balance	4.83~6.85	2.31~4.2	0.17	0.29 (max)

Table 2 Physical and mechanical properties of TC4 and CBN [30]

Parameters	Ti-6Al-4V	CBN
Thermal conductivity (W/(m·K))	6.8 (20 °C) 7.4 (100 °C) 9.8 (300 °C) 11.8 (500 °C)	1300
Density (kg/m ³)	4430	3480
Young's modulus (GPa)	109 (50 °C) 91 (250 °C) 75 (750 °C)	720
Poisson's ratio	0.34	0.16
Expansion coefficient (μm/m/K)	9.1	2.1
Specific heat (J/(kg·K))	611 (20 °C) 624 (100 °C) 674 (300 °C) 703 (500 °C)	670

$$\sigma = (A + B\varepsilon^n) \left(1 + C \ln \frac{\dot{\varepsilon}}{\dot{\varepsilon}_0} \right) \left[1 - \left(\frac{T_d - T_r}{T_m - T_r} \right)^m \right], \quad (1)$$

where σ is the equivalent stress; A is the quasi-static material yield strength; B is the strain hardening modulus; n is the strain hardening index; C is the strain rate hardening coefficient; m is the thermal softening coefficient; $\dot{\varepsilon}_0$ is the reference strain rate; T_d is the dynamic temperature of the material; T_m is the melting temperature of the material, and T_r is the environmental temperature of the material.

The J-C damage model is also utilized to explain the damage and fracture behavior of the material to characterize the damage parameters of TC4 alloy at high temperatures and high strain rates. When the failure parameter ξ in Eq. (2) is greater than or equal to 1, the material breaks and forms debris [28].

$$\xi = \sum \left(\frac{\Delta \bar{\varepsilon}^{p1}}{\bar{\varepsilon}^{p1}} \right), \quad (2)$$

$$\bar{\varepsilon}^{p1} = [d_1 + d_2 \exp(-d_3 \eta)] \cdot \left[1 + d_4 \ln \frac{\dot{\varepsilon}^{p1}}{\dot{\varepsilon}_0} \right] \left[1 + d_5 \left(\frac{T_d - T_r}{T_m - T_r} \right)^m \right], \quad (3)$$

where $\Delta \bar{\varepsilon}^{p1}$ is the equivalent plastic strain increment; $\bar{\varepsilon}^{p1}$ is the failure strain; $\dot{\varepsilon}^{p1}$ is the plastic strain rate; d_1 to d_5 are the failure constants and the J-C damage model parameters corresponding to TC4 are shown in Table 3 [31].

Table 3 J-C constitutive and damage model parameters of TC4 [31]

Variable	A (MPa)	B (MPa)	n	C	m
Parameter values	875	793	0.38	0.01	0.71
Variable	d ₁	d ₂	d ₃	d ₄	d ₅
Parameter values	-0.09	0.25	0.48	0.014	3.87

A semiconductor fundamental mode Gaussian laser is what is being used. For YAG pulsed lasers, the power density of the laser beam follows a Gaussian function distribution, and the mathematical expression for the energy density in one cycle is shown in Eq. (4).

$$I = \begin{cases} \frac{\alpha P}{\pi \tau f r_0^2} \exp\left(-\frac{2r_l^2}{r_0^2}\right), & 0 \leq t \leq \tau, \\ 0, & \tau < t < T, \end{cases} \quad (4)$$

where α is the absorption rate of the laser by the material; P is the output power of the pulsed laser; τ is the pulse width; f is the laser frequency; r_0 is the radius of the laser spot; r_l is the distance of the current position relative to the center of the laser source, and T is the period.

2.2 Removal Behavior Simulation

To minimize the size of the finite element model, the dimension of the workpiece is taken to be 0.15 mm × 0.06 mm × 0.04 mm, limiting the six degrees of freedom of the workpiece and making the bottom surface completely fixed. To ensure the calculation accuracy and improve the calculation efficiency, the mesh density of the scratched area is set to be higher (mesh size about 1 μm), and the mesh density of the other areas is set to be lower (mesh size about 3 μm), and the total number of cells after the division of the workpiece is 95200. The tip arc radius r_θ is 4 μm, and the angle of the abrasive taper is set to 60° [32]. The single abrasive tool is limited to five

directions at a predetermined horizontal speed v_w . The tool mesh is a four-node linear thermally coupled tetrahedral cell (C3D4T), tapering from the tip outwards, with a tip mesh size of approximately 1 μm and a total cell size of 7634 after tool division. The temperature of

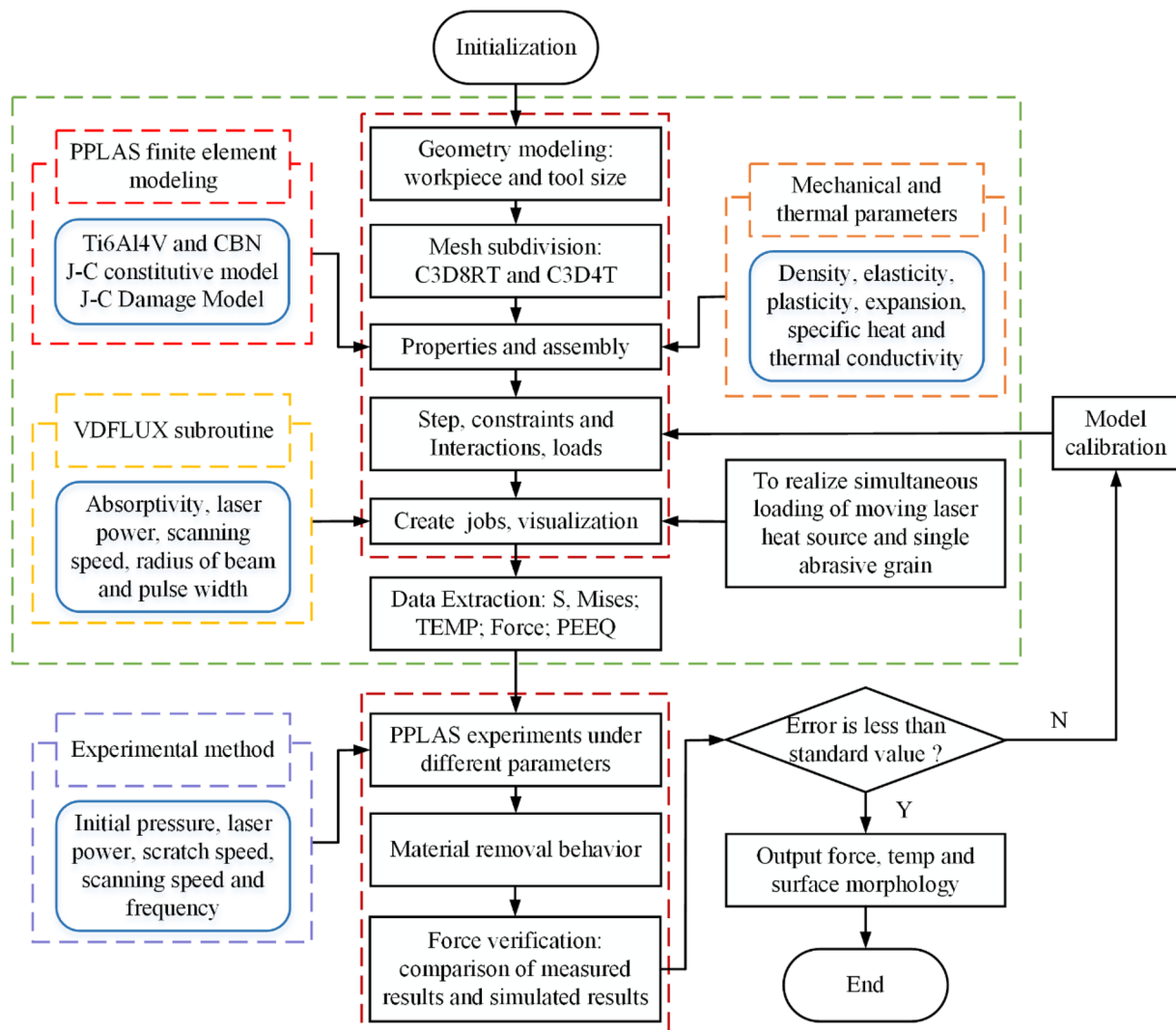


Figure 1 Flowchart of simulation analysis including four main steps: (1) Finite element modeling, (2) Establishment of pulsed laser heat source subroutine, (3) PPLAS experiments based on simulation optimization parameters, (4) Model calibration with force results

the tool and the workpiece is first fixed to 20 °C at room temperature. A moving surface heat flow is loaded on the upper surface of the workpiece and the relevant parameters are defined by the VDFLUX subroutine, as shown in Figure 1.

The VDFLUX moving heat source subroutine is created in Fortran, and parameters like the laser absorption rate of the TC4 alloy (0.34 [22]), laser power, scanning speed, spot radius, and pulse width are set to ensure simultaneous loading of the moving laser heat source and a single abrasive grain. The scratching speed v_w is set from 1 to 4 mm/s, the scratching depth a_p from 10 to 30 μm , and the laser power P from 2 to 8 W to investigate the impacts of various process parameters on the removal behavior of TC4.

Figure 2 shows the simulation results of the stress and temperature fields for different process parameters. During the scratching process, a portion of the material is subjected to the cutting action of the abrasive grain to generate a strip-shaped chip, and a portion of the material is squeezed to form a plastic bulge on both sides of the scratch. Besides, a different area of the material is affected by the high temperature between the tip of the abrasive grain and the material during the cutting process, causing J-C damage, resulting in the formation of thin and long chips, as shown in Figures 2a and b. Figures 2c and d show that the frictional heat produced by the extrusion of abrasive grains and scribing the surface of the workpiece, as well as the chip heat produced by the cutting action of abrasive grains, are the primary sources

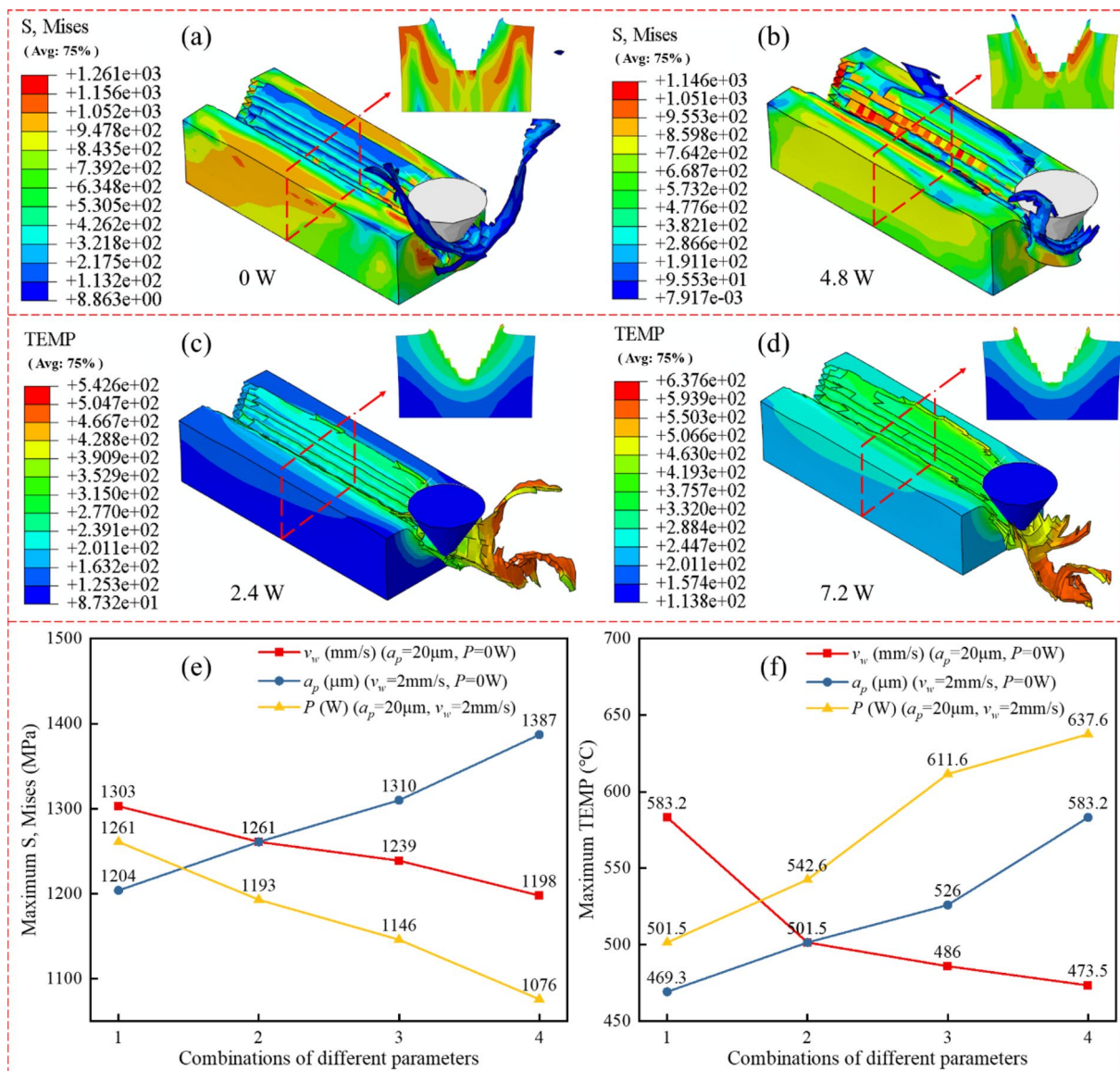


Figure 2 Simulation results of stress and temperature fields: **a-d** Different laser power ($a_p=20\ \mu\text{m}$, $v_w=2\ \text{mm/s}$), **e** Maximum values of S, Mises under different parameter combinations, **f** Maximum values of TEMP under different parameter combinations

of heat during the scratching process. The high-temperature areas are mainly distributed on the tips of the abrasive grains in contact with the workpiece, the strip-shaped abrasive debris, and the slender debris generated during the scratching process.

From Figures 2e and f, it can be seen that the von Mises stress and unit temperature both gradually decrease with the increase of scratching speed, reaching the minimum values, 1198 MPa, and 473.5 °C, respectively, when the scratching speed is 4 mm/s, with a maximum decrease of 8.06% and 18.81%, respectively. As the scratching depth increases, both the von Mises stress

and unit temperature gradually increase, reaching maximum values at a scratching depth of 28 μm , 1387 MPa, and 583.2 °C, respectively, with a maximum increase of 15.20% and 24.27%. The von Mises stress gradually decreases as the laser power increases, reaching a minimum value of 1076 MPa, at a laser power of 7.2 W, with a maximum decrease of 14.67%. The unit temperature increases with the increase of laser power, increasing by 14.59%, 29.17%, and 34.66% during PPLAS compared with CS at the same scratching depth. The maximum value (637.6 °C) is reached when the laser power is 7.2 W, which is below the melting point of TC4.

Through the above analysis, the impacts of scratching speed on the form of debris, scratching morphology, temperature field, and stress field distribution during TC4 material removal process are less than that of laser power and scratching depth. Therefore, the subsequent experimental validation mainly explores the effects of laser power and scratching depth on the removal behavior of TC4 during PPLAS.

3 Experiment Details and Methodology

PPLAS experiments are carried out to verify the simulated results of material removal behavior under different process parameters. In this section, the experimental setup, experimental parameters, and detection methods are described in detail. Meanwhile, the simulation results of TC4 material removal at corresponding scratching depths are verified by scratching experiments under different initial pressure.

3.1 Experimental Setup

PPLAS experiments are conducted on a laser belt machining device developed by the team, as shown in Figure 3a. The abrasive grains used in the experiments are cubic boron nitride (CBN) abrasive grains with the physical property parameters shown in Table 2, which are welded to the bottom of the tool using metallurgical powder. The microscopic morphology of the CBN abrasive grain is obtained by the VHX-1000C ultra-deep field 3D microscope system from KEYENCE, the 3D morphology at 100× magnification is shown in Figure 3b, and the surface of the machined TC4 workpiece is shown in Figure 3c. The parameters of the picosecond pulse laser used for the experiments are shown in Table 4.

3.2 Experimental Method

The indentation depth of a single abrasive grain cannot be precisely controlled due to the repeatability

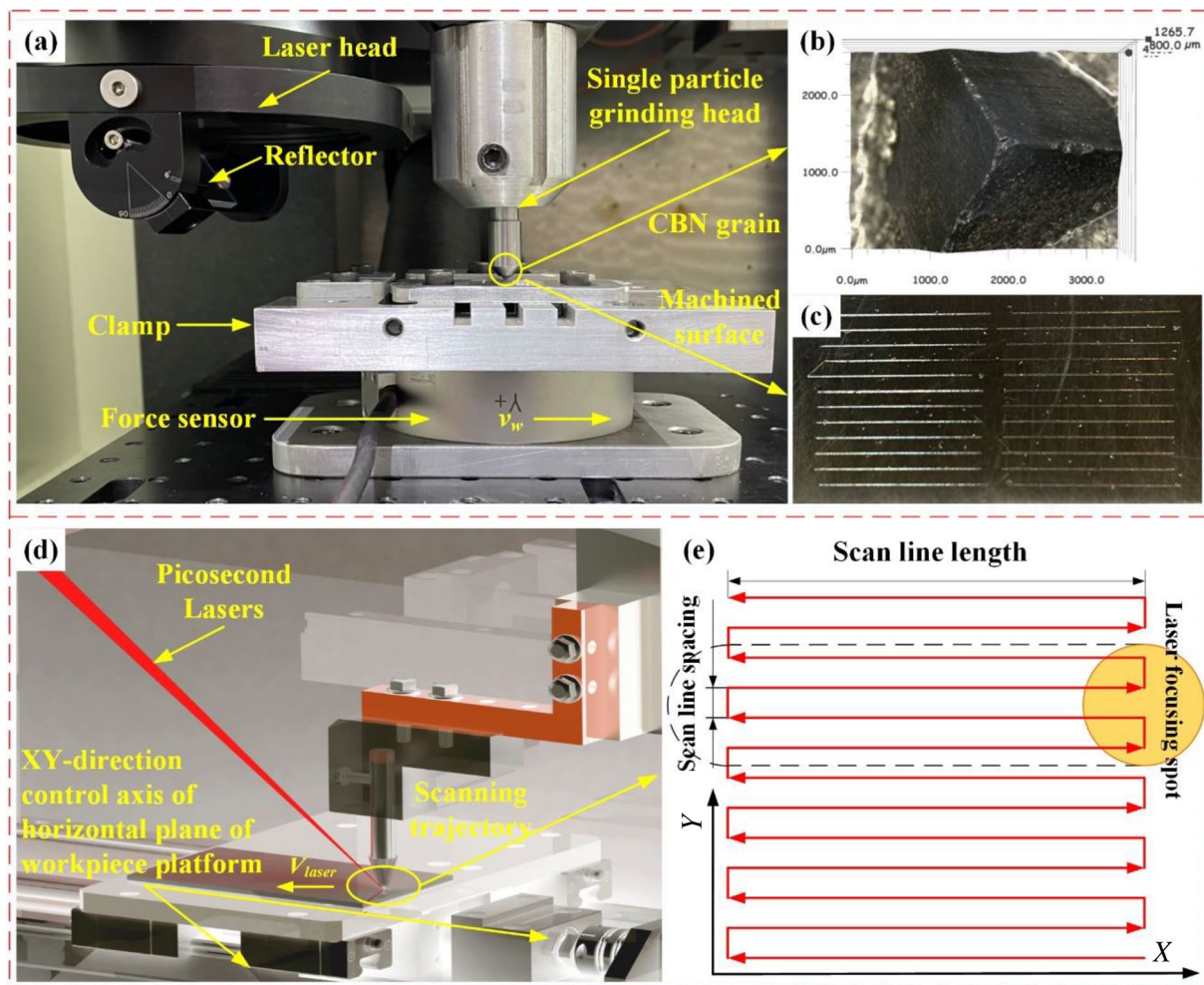


Figure 3 Experimental platform for PPLAS: **a** Overall experiment setup, **b** CBN abrasive grain, **c** Machined workpiece, **d** 3D model of the experimental device, **e** Laser scanning path

Table 4 Picosecond pulse laser performance parameters

Parameters	Description
Wavelength (nm)	1064
Maximum power (W)	12
Pulse width (ps)	13
Spot diameter (μm)	30
Frequency (kHz)	100~2000
Beam quality factor (M^2)	< 1.3
Fundamental mode	TEM ₀₀

and positioning accuracy of the experimental setup of $\pm 18 \mu\text{m}$ and $\pm 20 \mu\text{m}$. Therefore, this experiment is carried out by controlling the initial pressure of the single abrasive grain for different scratching depths. In combination with the simulated results in Section 2.2, the initial pressure of 6 N, 9 N, 12 N, and 15 N are selected according to the grinding depths of the single abrasive grains used in the study by Liu et al. [33]. Additionally, the laser power of 0 W, 2.4 W, 4.8 W, and 7.2 W are selected, the scratching speed is 2 mm/s, the scanning speed is 1000 mm/s and the frequency is 2000 kHz. To ensure that the laser irradiation region completely covers the scratching area and that there is no contact between the scratches, the laser scanning path width is adjusted to 1 mm and the scratch spacing to 1.5 mm. The scanning path is shown in Figure 3e.

For the acquisition and examination of grinding force, a Kistler 9256C1 force measuring equipment with accuracy and sampling frequencies of 0.1 N and 1000 Hz is used. A white light interferometer is used to observe the surface morphology of the scratch with a sampling area of $1.11 \text{ mm} \times 0.89 \text{ mm}$ and three different areas before, during, and after the scratch are examined for each set of machining parameters. The surface morphology and debris distribution are observed using field emission scanning electron microscopy (SEM; Quattro S, America), the elemental content and distribution of the workpiece surface are measured using energy spectrometry (EDS; Quattro S, America), and the temperature field of the machining process is measured by the thermal imager (Fluke Ti90, America).

4 Results and Discussion

Based on the above simulation analysis and experimental setup, the dynamic material removal process of TC4 is clarified by the comparison of simulated and measured results. In addition, the impacts of process parameters on the removal behavior of TC4

are analyzed in detail from five aspects: temperature field, grinding force, material removal degree, surface topography, and the form of debris, and corresponding discussions are carried out.

4.1 Experimental Detection of Temperature Field

The temperature field during PPLAS is observed to fluctuate less when different parameter combinations are used with a thermal imaging camera, thus the same parameter combinations of the simulation are used to study the temperature field in laser-assisted belt grinding. An alumina abrasive belt with a grain size of 60 is used in a laser-assisted belt grinding experiment on a titanium alloy plate, and a belt line speed of 3.75 m/s is chosen to record the temperature in the center. The temperature at the edge of the contact wheel and workpiece contact area is taken as the test result, as shown in Figure 4.

As can be observed from Figure 4a, the temperature steadily drops as the feeding speed rises. And it reaches a minimum value of $67.4 \text{ }^\circ\text{C}$ when the feeding speed is 4 mm/s. From Figure 4b, it can be seen that the temperature rises steadily with the increase of initial pressure, reaching a maximum value of $90.9 \text{ }^\circ\text{C}$ in the middle area at an initial pressure of 15 N. From Figure 4c, it can be found that the temperature increases continuously as the laser power increases, and the temperature under different laser power of laser-assisted belt grinding increases by 10.79%, 16.38%, and 28.41%, respectively, compared with conventional belt grinding under the same initial pressure. When the laser power is 7.2 W, the temperature in the detected region reaches a maximum value of $103.5 \text{ }^\circ\text{C}$. The trend is consistent with the simulated results in Figure 2f. As can be seen in Figure 4, the irradiation of the workpiece by the laser in front of the contact wheel results in a larger area of high-temperature field distribution than under conventional belt grinding. One possible reason for this is that the thermal-mechanical coupling effect is weakened with laser heating in the grinding area.

4.2 Grinding Force

During the scratching process, the grinding force can be divided into three mutually perpendicular components: normal grinding force, tangential grinding force, and axial grinding force. The axial grinding force generally has a low value and is not considered in studies [34]. The measured and simulated results of the grinding force variation curves for different laser power and initial pressure at a scratching speed of 2 mm/s and a scanning speed of 1000 mm/s are shown in Figure 5. It can be found that the amplitude of the simulated signal is greater than the experimentally measured signal, and the initial

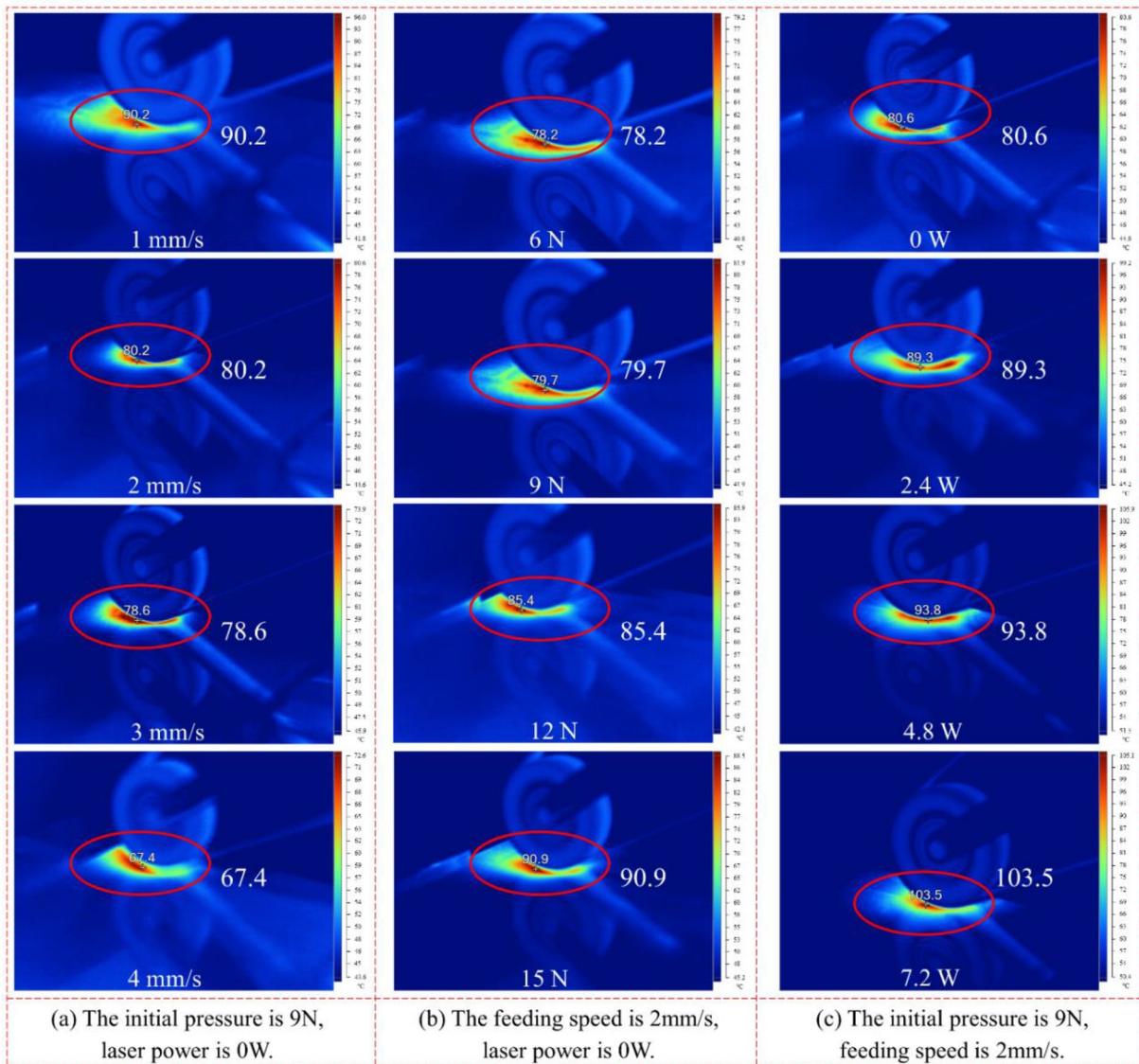


Figure 4 Temperature field detection results under different process parameters: **a** Different feeding speed ($F_p=9\text{ N}, P=0\text{ W}$), **b** Different initial pressure ($v_w=2\text{ mm/s}, P=0\text{ W}$), **c** Different laser power ($F_p=9\text{ N}, v_w=2\text{ mm/s}$)

part of each curve, where the grinding force reaches its maximum value for a small period, corresponds to the transient phase of chip formation in the metal cutting process. When the grinding process settles, the grinding force fluctuates up and down within a certain range, and tends to be stable eventually. This is mostly due to the continuous fracture and formation of debris during the grinding process.

As shown in Table 5, the error rate is calculated as the ratio of the absolute value of the difference between the experimental grinding force and the simulated grinding force to the experimental grinding force. The error in the experimental and simulated grinding force signals,

as demonstrated, is within 12%, indicating that the simulated force signal and the measured force signal are in good agreement.

The grinding force and error rates at different laser power and initial pressure are compared in Figure 6 using experimental measurements and simulated results. Both CS and PPLAS results demonstrate that the grinding force increases with the increase of initial pressure. An increase in the initial pressure causes the single abrasive's depth of indentation to rise, which in turn leads to an increase in the rubbing depth, undeformed chip thickness, and grinding force. At the same initial pressure, the grinding force during PPLAS is lower compared with

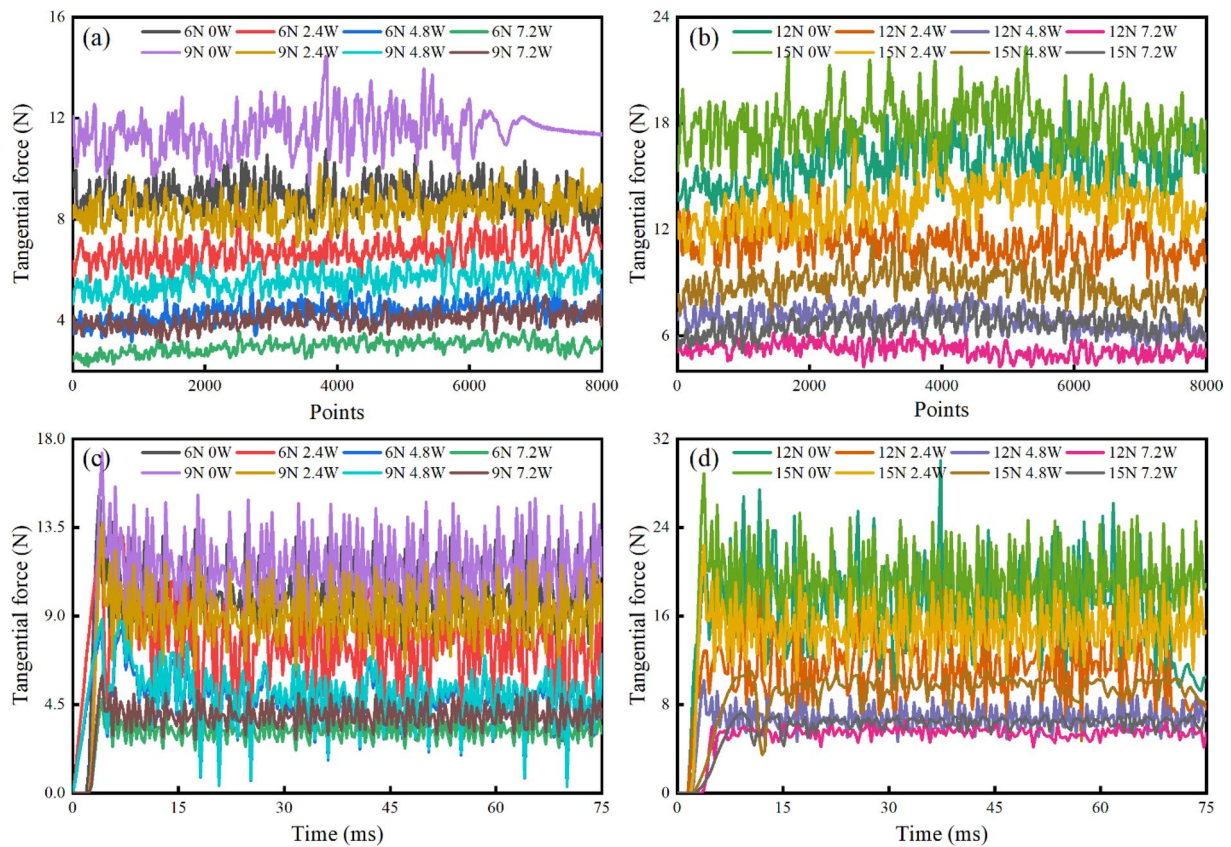


Figure 5 Comparison of grinding force signal measurements and simulations at different laser power and different initial pressure: **a, b** Measured signal; **c, d** Simulated signal

Table 5 Comparative analysis of tangential grinding force detection and simulation results at different laser power and different initial pressure

Initial pressure (N)	Laser power (W)	Tangential force F_t (N)		
		Measured results (Averaged value for three times)	Simulated results	Error rate (%)
6	0	8.90	9.82	10.33
6	2.4	6.74	7.52	11.57
6	4.8	4.36	4.73	8.49
6	7.2	2.97	3.14	5.72
9	0	11.49	11.04	3.92
9	2.4	8.41	9.03	7.37
9	4.8	5.57	4.98	10.59
9	7.2	4.05	3.93	2.96
12	0	15.60	16.20	3.85
12	2.4	11.24	10.04	10.68
12	4.8	6.92	6.75	2.46
12	7.2	5.21	5.05	3.07
15	0	17.88	19.09	6.77
15	2.4	13.35	14.84	11.16
15	4.8	8.89	9.22	3.71
15	7.2	6.61	5.98	9.53

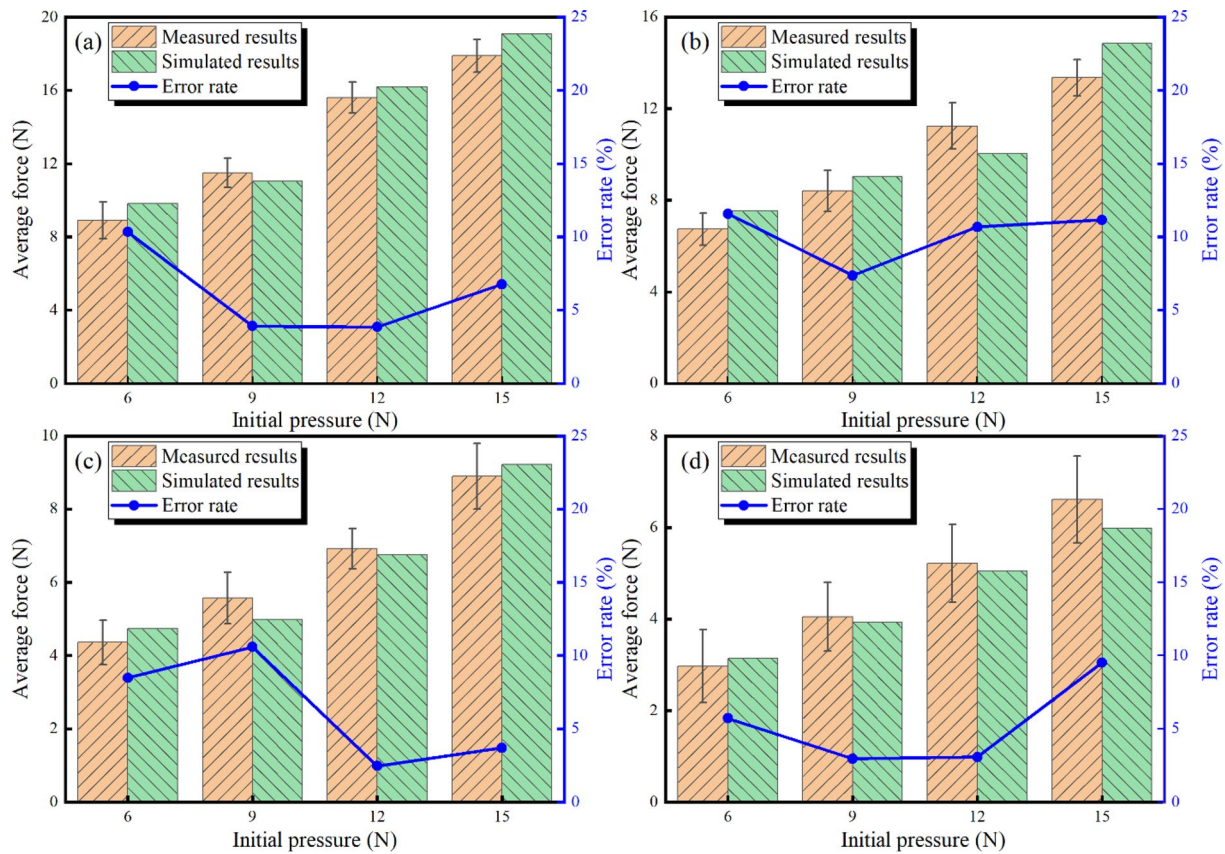


Figure 6 Comparison of experimental measurements and simulated results of grinding force at different laser power and initial pressure and their error rates: **a** 0 W, **b** 2.4 W, **c** 4.8 W, **d** 7.2 W

CS, and the grinding force decreases with the increase of laser power. A similar phenomenon is also found in the study by Zhang et al. [35]. When the laser power is 7.2 W, the tangential grinding force under different initial pressure drops to the lowest value, from 8.90 N, 11.49 N, 15.60 N, and 17.88 N during CS to 2.97 N, 4.05 N, 5.21 N, and 6.61 N, respectively, a decrease of 66.62%, 64.75%, 66.60%, and 63.03%. From the previous analysis of the temperature distribution, it is clear that the higher the laser power, the higher the surface temperature of the material. Moreover, the softening effect is enhanced, and both the surface hardness of the material and the grinding force decrease.

4.3 Material Removal Degree

The cross-sectional profile of CS at different initial pressure is shown in Figure 7. The scratching width and depth grow as the initial pressure rises, with widths of 0.07 mm, 0.08 mm, 0.09 mm, and 0.10 mm and depths of 15 μm, 20 μm, 25 μm, and 28 μm, respectively.

As shown in Figure 8, the cross-sectional area of material accumulation on both sides of the scratch is S_1 and the cross-sectional area of the scratch is S_2 . According

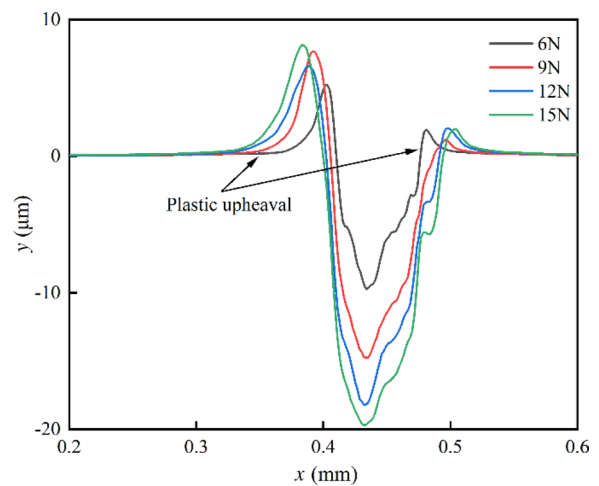


Figure 7 Cross-sectional profile of CS at different initial pressure

to the method from Hokkirigawa et al. [36], the material removal degree λ during single abrasive grinding can be calculated by the equation $\lambda = (S_2 - S_1) / S_2$.

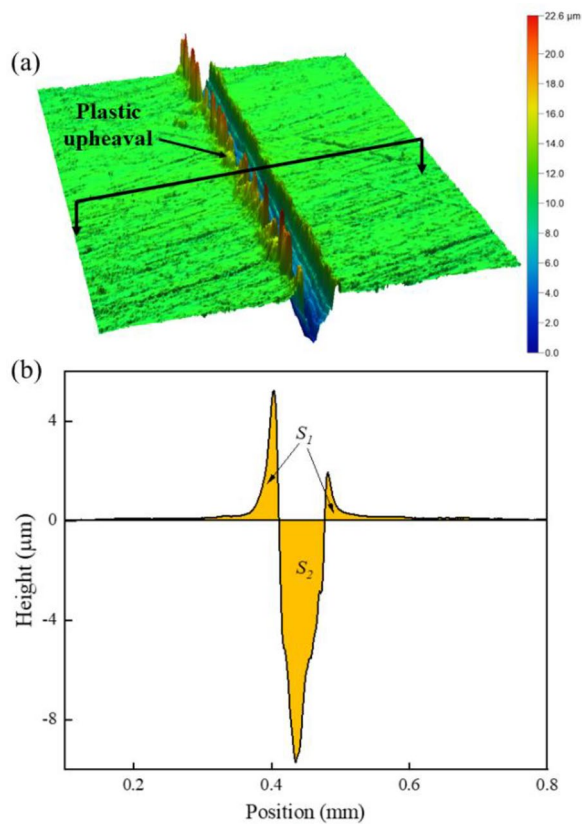


Figure 8 Scratch cross-sectional profile: **a** three-dimensional topography of white light detection, **b** the middle section profile of **a**, where S_1 is the cross-sectional area of material accumulation on both sides of the scratch, and S_2 is the cross-sectional area of the scratch

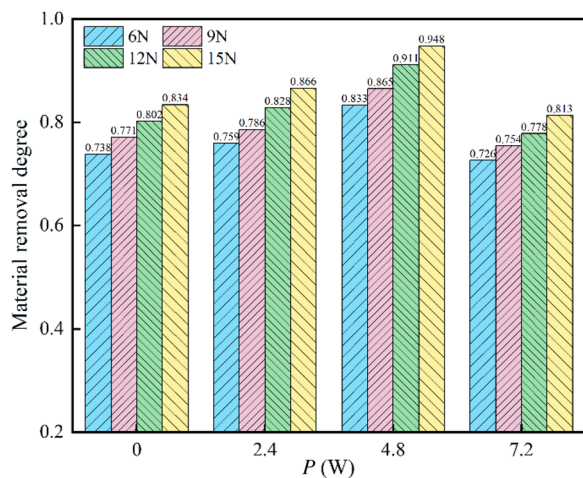


Figure 9 Variation of material removal degree with laser power at different initial pressure

Figure 9 shows the trend of the material removal degree λ with laser power for different initial pressure with a scratching speed of 2 mm/s and a laser scanning speed of 1000 mm/s. As can be seen from Figure 9, the value λ becomes larger with the increase of the initial pressure for both CS and PPLAS. This indicates that the material removal capability of the single abrasive grain becomes stronger as the scratching depth increases. The single-grit material removal process can be divided into the following three stages: slip rubbing, ploughing, and cutting. Under the squeezing effect of the abrasive grains, the workpiece material generates plastic flow. Meanwhile, the ploughing effect gradually decreases with the increase of the initial pressure, which enhances the material removal capacity under single-grit cutting.

At different initial pressure, the value λ tends to increase and then decrease as the laser power increases. At a laser power of 4.8 W, the value λ reaches a maximum of 0.948. When the laser power is low, the laser radiation is applied to the material surface to soften the material and improve its machinability, thus improving the material removal and increasing the value λ . With the further increase of laser power, the “softening effect” of the material becomes more pronounced and the degree of plasticity is further increased, but due to the negative front angle of the abrasive grain cutting, the abrasive grain is extruded on the surface of the workpiece and the processing grooves are scored. The plastic deformation of the material at the front of the grain results in the material being squeezed and flowing to both sides of the grain, resulting in a gradual reduction of the value λ . When the laser power reaches 7.2 W, the value λ during PPLAS is reduced by a maximum of 14.60% compared with CS.

According to the examination of the preceding data for grinding force and material removal degree, both the grinding force and the material removal degree decrease as the laser power increases. Therefore, when selecting the values of laser power, attention needs to be paid to the mutually limiting relationship between the grinding force and the material removal degree.

4.4 Material Removal Profile

Figure 10 shows the results of the 3D morphological inspection and simulation of CS at different initial pressure. It can be seen that during the scratching process, the titanium alloy plastic flow occurs and rises slightly on both sides of the scratch, and a portion of the material is extruded due to the plastic shear flow, which is removed or flattened at the edge of the scratch by the abrasive grains. With the increase of the initial pressure, the distance from the highest point to the lowest point of

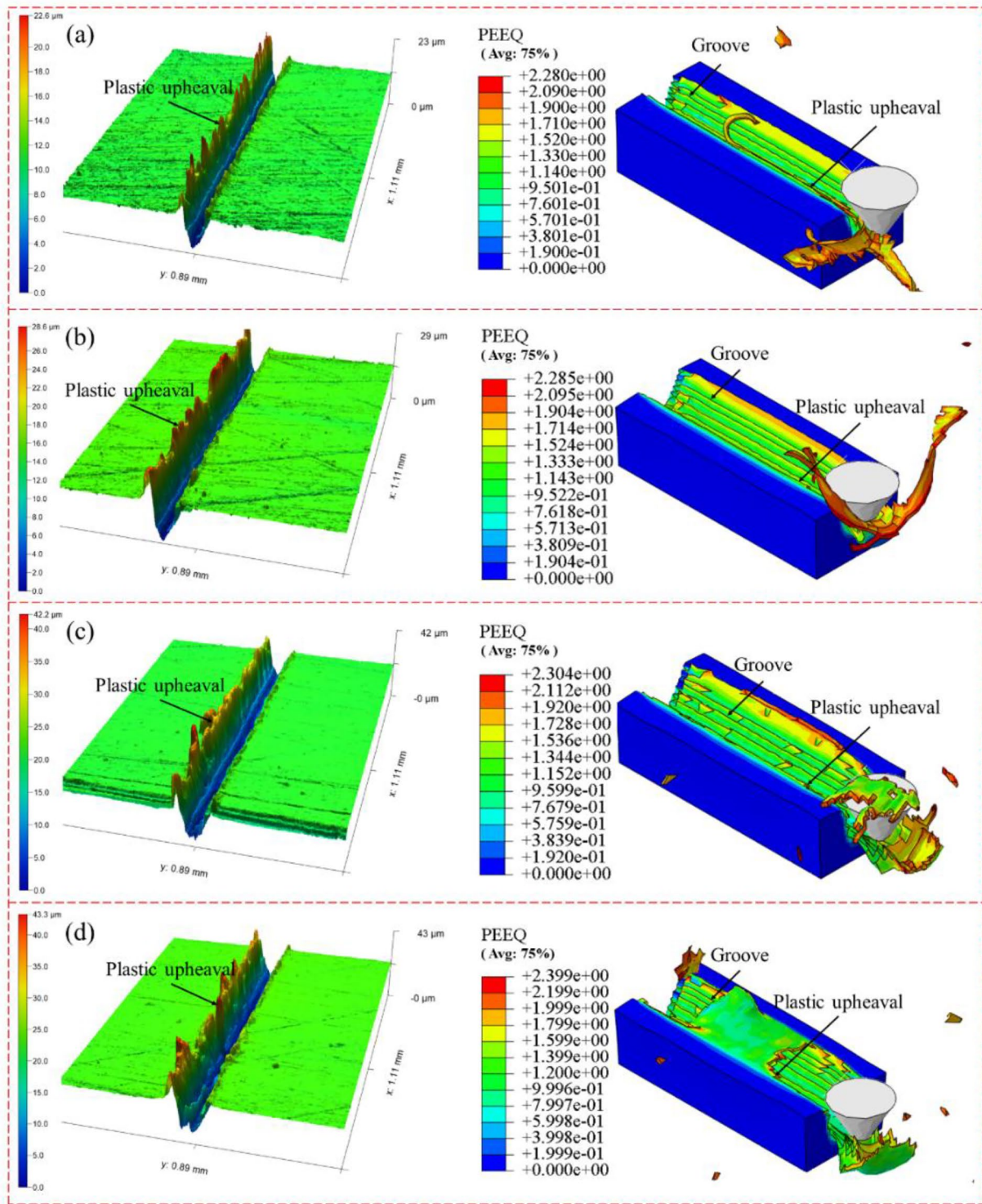


Figure 10 Detected and simulated results of CS surface topography under different initial pressure: **a** 6 N, **b** 9 N, **c** 12 N, **d** 15 N

the scratch surface gradually increases, and the equivalent plastic strain also shows a gradually increasing trend. This is mainly because the increase of the initial pressure

leads to an increase in the indentation depth of the abrasive grains. The scratching depth also increases, the plastic flow phenomenon and the plastic shearing effect of

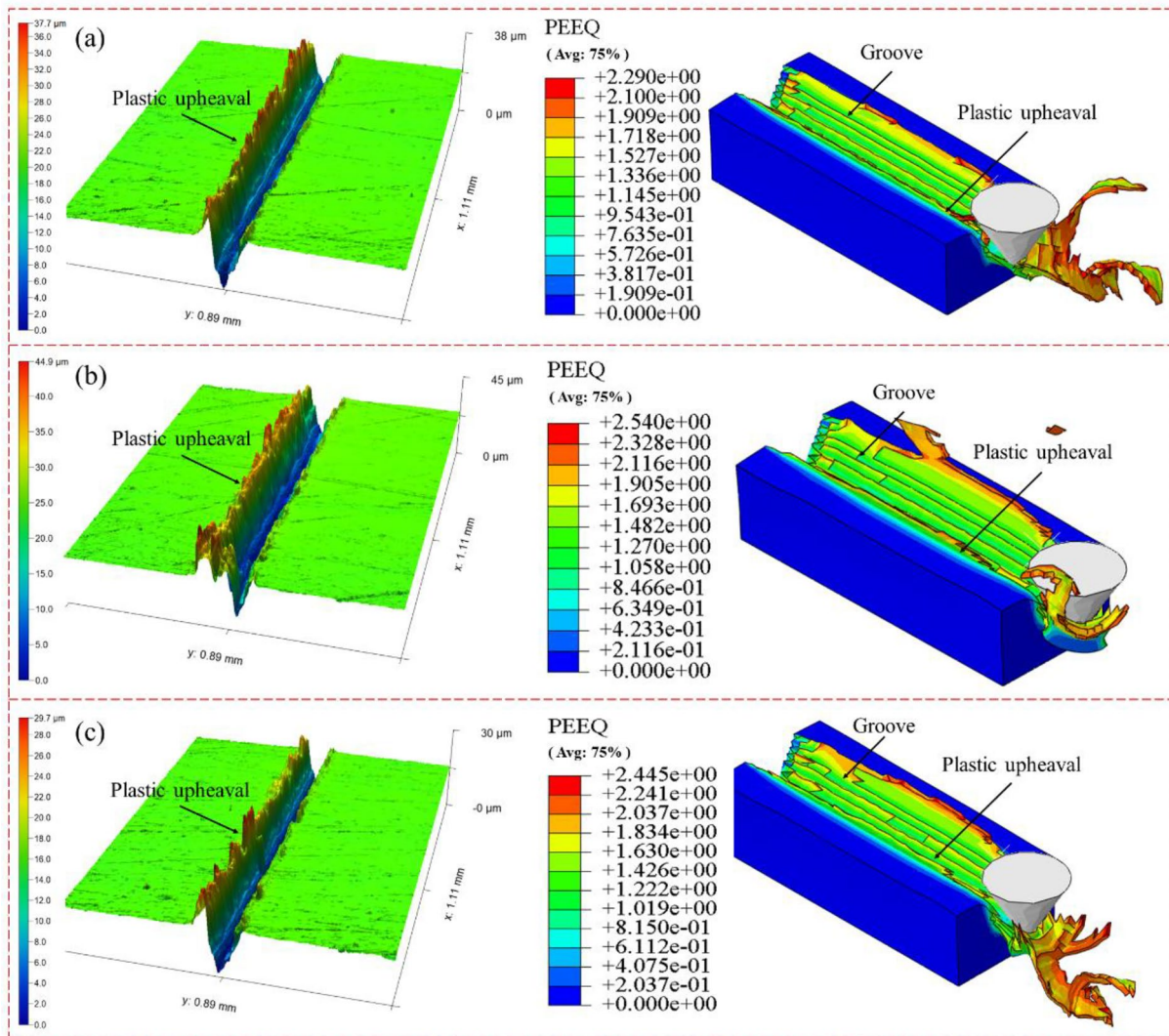


Figure 11 Scratch surface topography and simulation results at different laser power: **a** 2.4 W, **b** 4.8 W, **c** 7.2 W

the abrasive grains on the material are enhanced, and the degree of wear on the scratch surface increases, producing small grooves.

Taking the initial pressure as 9 N, the 3D morphological inspection and simulation results of the scratch surface under different laser power are compared, as shown in Figure 11. It can be seen that with the increase of laser power, the distance from the highest point to the lowest point of the scratched surface shows a trend of first increasing and then decreasing, which is consistent with the trend of the equivalent plastic strain during the simulation. This indicates that the plastic deformation capacity of the material increases after laser irradiation, and the plastic upheaval on both sides

of the scratch increases. However, the bulge on both sides of the scratch decreases compared with the laser power of 4.8 W when the laser power reaches 7.2 W. One of the possible reasons for this is that the material is softened with laser heating and is cut off before significant deformation occurs.

4.5 Removal Behavior Analysis

Figure 12 shows the results of scratch morphology inspection of CS at a scratching speed of 2 mm/s and an initial pressure of 9 N. From Figure 12a, it can be seen that under the action of the abrasive grains, the material undergoes plastic deformation, part of which forms debris through the extrusion of the front end of the abrasive grains, and

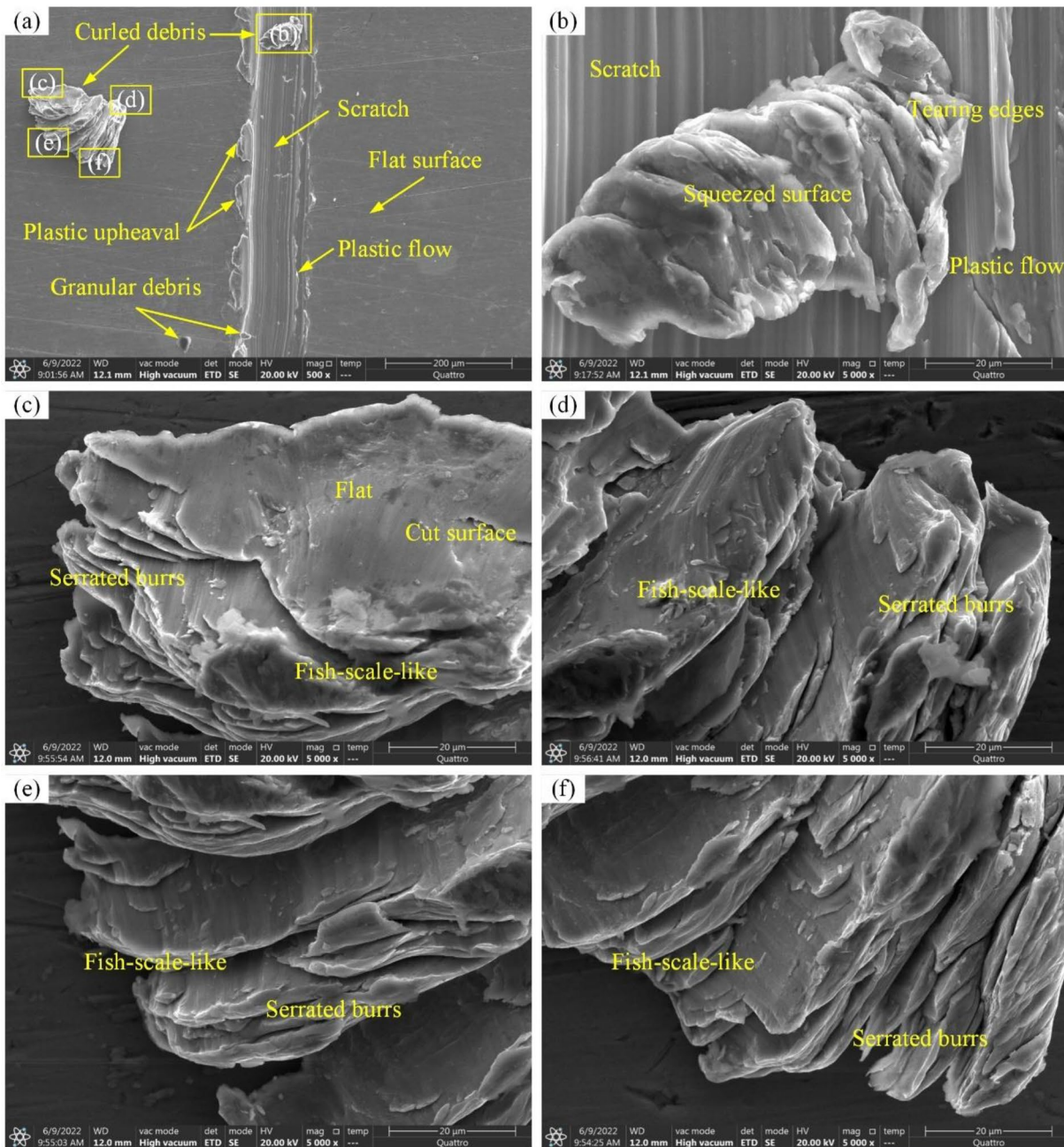


Figure 12 Surface characterizations after CS under $v_w = 2$ mm/s and $F_p = 9$ N: **a** Conventional scratches and shapes, **b–f** are enlarged views of the areas indicated in **a**

part of which flows to the sides of the scratch to form plastic upheaval. During the abrasive grain cutting process, the TC4 material is separated from the titanium alloy surface in the form of flakes under the extrusion of the abrasive. Due to the ductility of the TC4 material and the high temperature generated by the abrasive scratch, the material softens so that as the abrasive grains move forward, these “flakes” bond together layer by layer, eventually forming a curved

strip of abrasive chips. A similar phenomenon was seen in the studies [37, 38]. Before the abrasive grain cutting, the relatively smooth side of the workpiece surface is located below the “fish scale” surface and is in direct contact with the abrasive grain during the cutting process. The upper “fish scale” surface is scratched by the abrasive grains, and there are multiple scratches on the surface, which explains the unevenness of the “flakes” edges shown in Figures 12b–f.

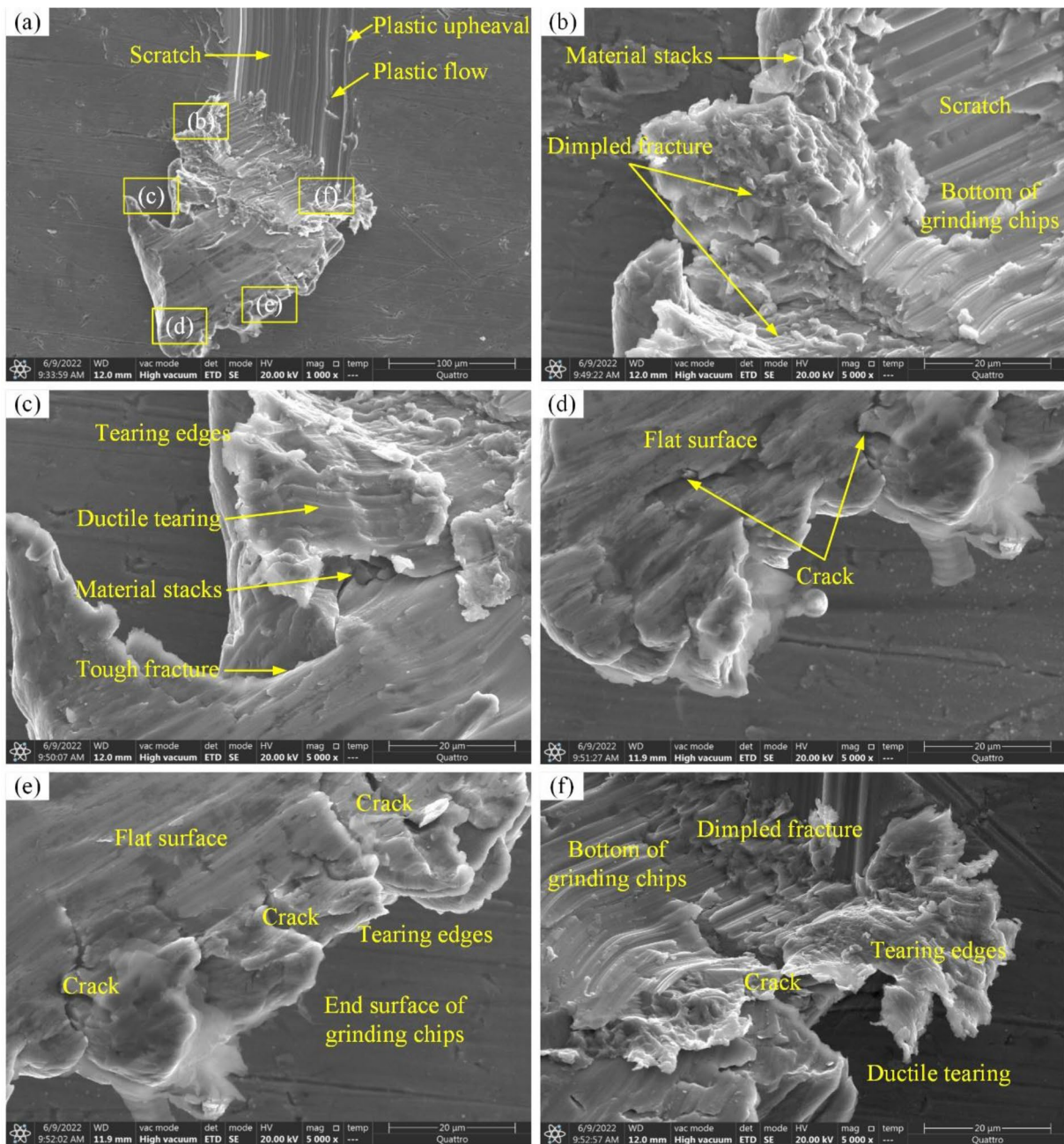


Figure 13 Surface characterizations after PPLAS under $v_w = 2$ mm/s, $F_p = 9$ N, and $P = 0$ W: **a** laser-assisted scratches and morphology, **b–f** are enlarged views of the areas indicated in **a**

Figure 13 shows the results of PPLAS scratch profile at a scratching speed of 2 mm/s, a scanning speed of 1000 mm/s, an initial pressure of 9 N, and a laser power of 7.2 W. Figure 13a shows the overall schematic of the shape and its abrasive chips during PPLAS. It can be seen that the workpiece material is plastically deformed by the action of the abrasive grains and plastic flow is generated on the surface, but the plastic upheaval on both sides of

the scratch is reduced compared with that generated by the single abrasive scratch in Figure 12. In addition, during the PPLAS process, fractured serrated chips appear at the end of the scratch, unlike the stacked chips that appear during the CS process. The possible reason for this is that the material is softened by laser heating and the material becomes easier to remove. As can be seen from the previous analysis of the grinding force results, the tangential

force at this point is 4.05 N, which is 64.75% lower than that of the single abrasive scratching (tangential force of 11.49 N) with the same parameters. Figures 13b–f show a partial magnification of the abrasive chip, from which it can be seen that the root of the chip can be divided into three parts: the bottom of the chip, the chip-substrate separation zone and the scratching surface. During the separation process, the abrasive chips will rub against the

front surface of the tool of the abrasive grains, thus producing irregular abrasive marks on the chip surface and distributing uneven fracture structures in the separation area, from which morphological features such as tearing of the workpiece material and tough nests of material toughness fracture can be observed. This result indicates that the removal form of TC4 alloy in the PPLAS process is still plastic extrusion removal.

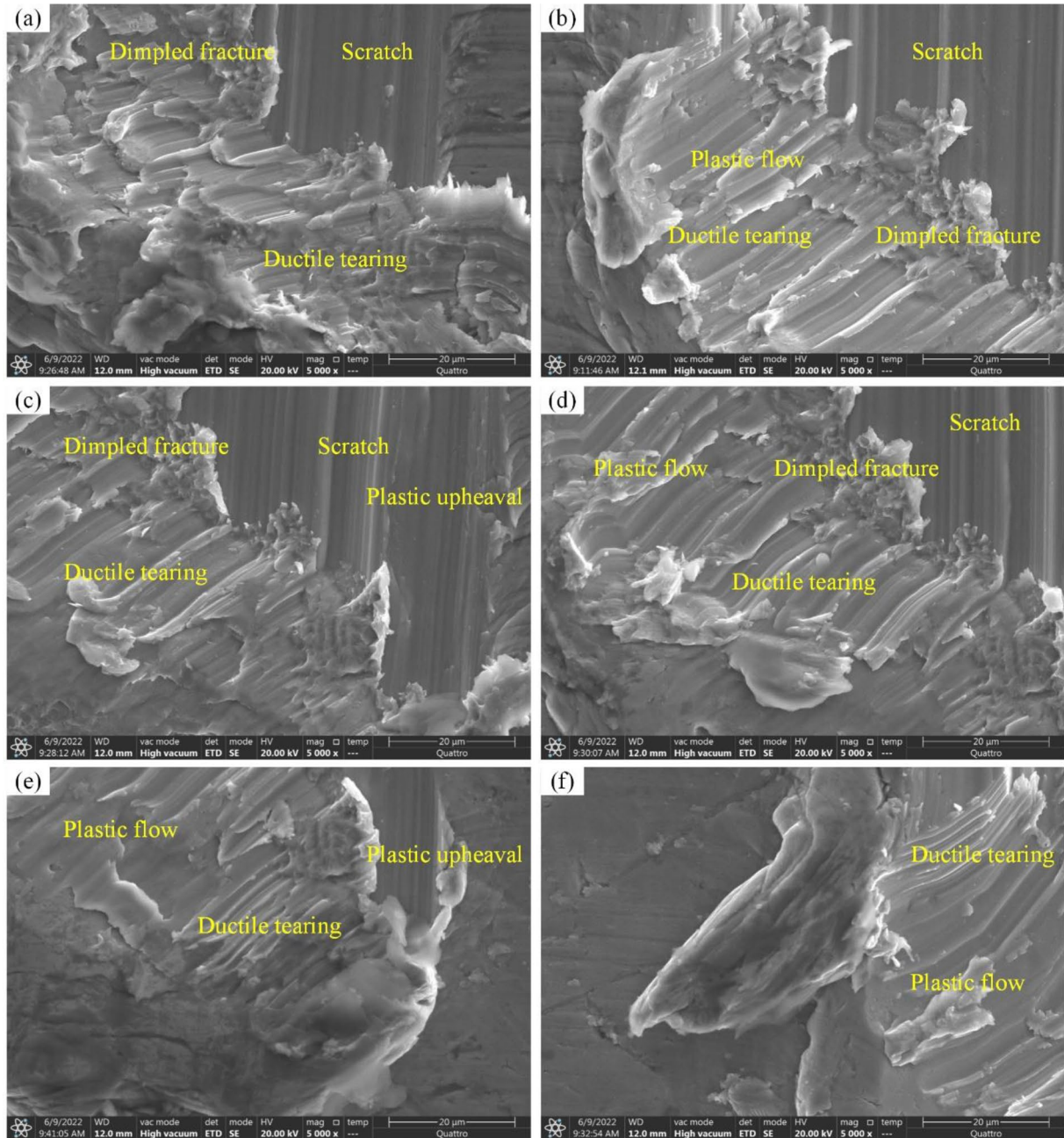


Figure 14 Scratched end detection results under different initial pressure and different laser power: **a** 6 N, **b** 6 N 4.8 W, **c** 12 N, **d** 12 N 4.8 W, **e** 15 N, **f** 15 N 4.8 W

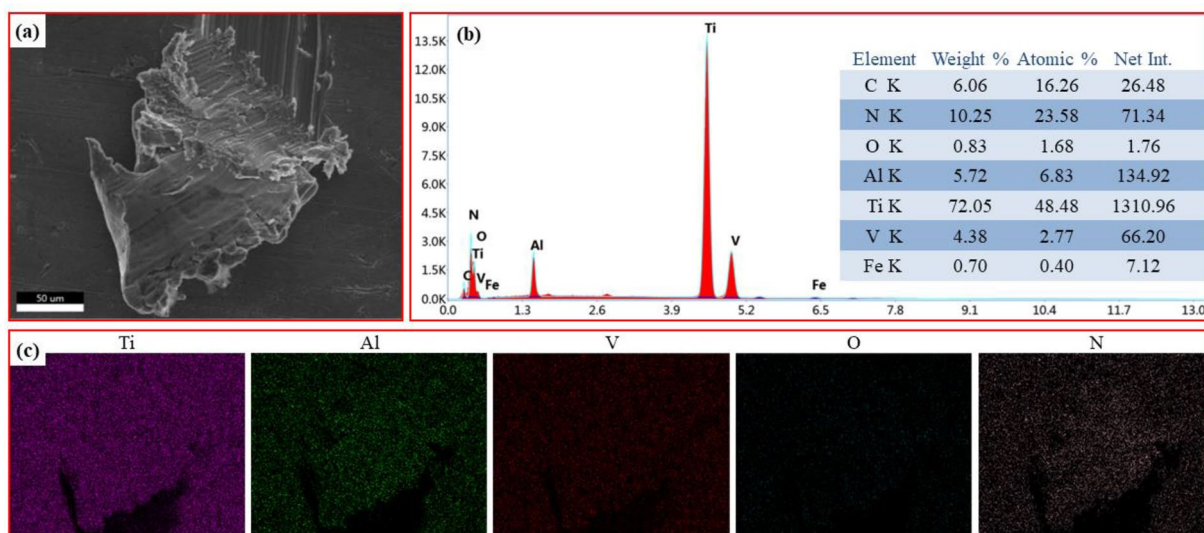


Figure 15 Energy spectral results of Figure 13a: **a** Scratching end, **b** Surface energy spectral results and element content, **c** Element distribution

It is found that the plastic deformation of the workpiece material under the effect of the laser irradiation is reduced and the chip-substrate separation zone at the scratch end is different from the CS. To further investigate the effect of different initial pressure and the presence or absence of laser power on the chip-substrate separation zone, a laser power of 4.8 W at the maximum material removal degree is selected, and six different combinations of parameters are used to examine the shape of the scratch end. As can be seen from Figures 14a, c and e, as the initial pressure increases, the indentation depth of the single abrasive grain increases, which leads to an increase in the scratch depth and the degree of plastic deformation. This in turn causes an increase in the degree of plastic flow and plastic deformation, and morphological features such as tearing of the material and tough nests of the material fracture appear in the chip-substrate separation zone. It can be seen from Figures 14b, d and f that the surface of the workpiece material is heated by the laser, which softens the material and makes it easy to remove, resulting in less plastic flow and less ductile tearing in the chip-substrate separation zone.

The results of the surface energy spectroscopy analysis of the scratched area at the laser power of 7.2 W in Figure 13a are shown in Figure 15. Compared with the original elemental distribution of TC4 alloy in Table 1, the laser-assisted single-grit scratching area shows a significant increase in carbon and nitrogen elements, a small increase in oxygen and iron elements, and uniform distribution of alloying elements. This result indicates that the increase in elemental content is due to the oxidation of titanium and aluminum elements in TC4 alloy in air,

rather than the oxidative modification [39, 40] or ablation [41, 42] of the material surface by the high-energy laser irradiation, which indicates lower damage to the unscratched area during PPLAS.

Combined with the results of the above analysis, the material removal mechanism of TC4 alloy under CS and PPLAS is clearly illustrated in Figure 16. As the initial pressure increases, the abrasive grain is pressed further into the workpiece, and the sidewalls of the grooves are raised as a result of the material's plastic slip, forming the plastic upheaval. As the squeezing depth of the abrasive grain continues to increase, the area being squeezed by the grain slips significantly, and chips are formed to flow out of the front tool face of the grain to form the cutting stage. During the CS process, a portion of the material is squeezed due to the plastic shear flow, which is removed or flattened at the edge of the scratch by the abrasive grinding, and a portion of the material is cut by the abrasive to form a thin strip of chips. The material is subjected to abrasive grain cutting during the PPLAS process, resulting in the formation of fine ribbon chips. This is mainly due to the effect of laser irradiation, which increases the surface temperature of the workpiece material, softening the material and increasing the degree of plastic deformation. Under high temperatures, the raised material is crushed finer, eventually forming thin and long flakes.

5 Conclusions

In this study, a PPLAS method considering both the temperature-dependent material properties and the ultrashort pulse laser's characteristics is proposed. The

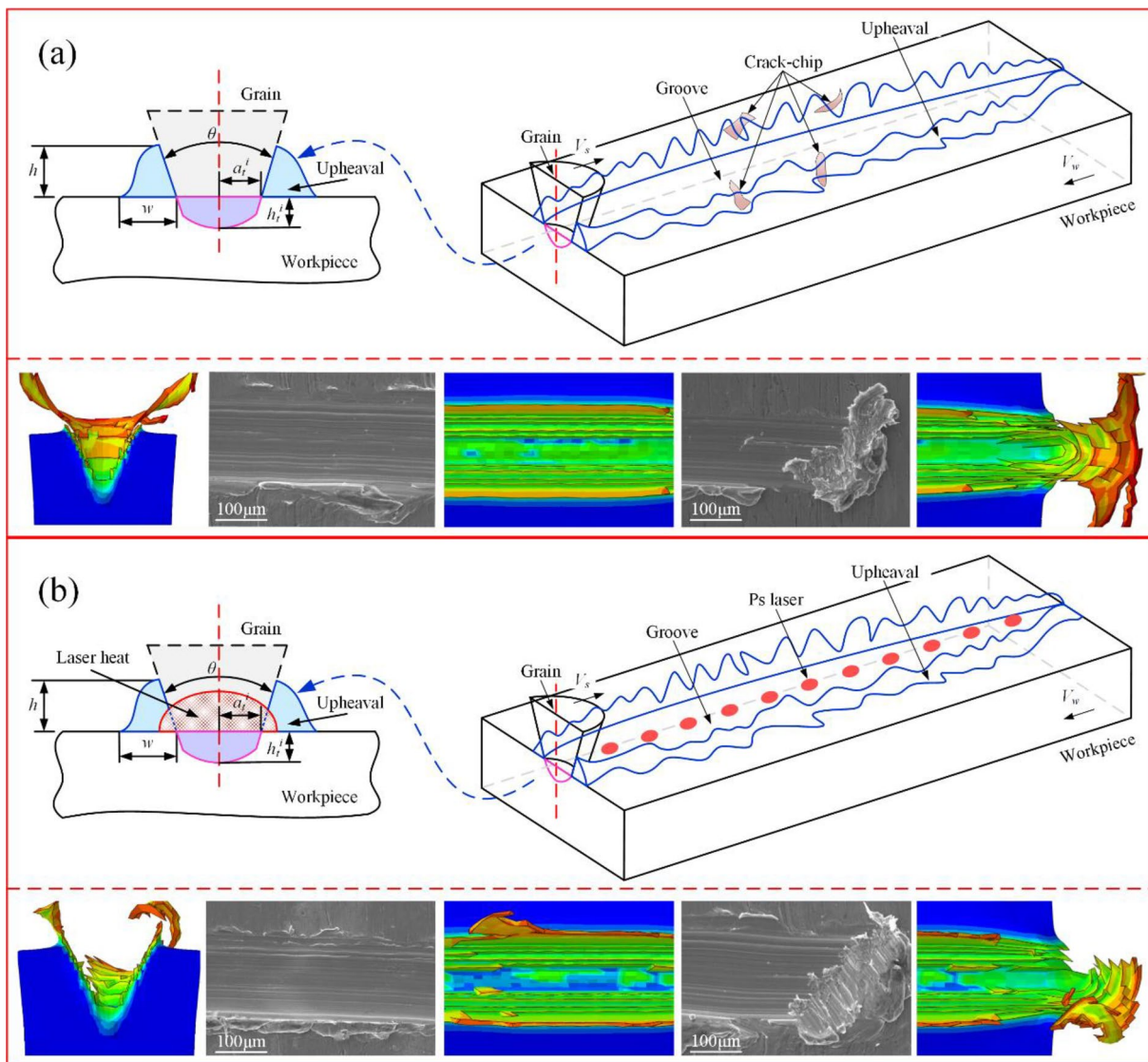


Figure 16 Schematic diagram of the TC4 alloy removal mechanism: **a** CS, **b** PPLAS

distribution of the stress field, temperature field, and equivalent plastic strain during CS and PPLAS are then analyzed with simulated results. Furthermore, the grinding force and material removal behavior are evaluated by PPLAS experiments compared with CS. The conclusions of the study can be summarized as follows:

- (1) In PPLAS of TC4, the von Mises stress has a positive correlation with scratching depth and a negative correlation with laser power and scratching speed. When the laser power is 2.4, 4.8, and 7.2 W, the maximum temperature increases by 14.59%, 29.17%, and 34.66%, respectively, compared with that of CS at the same scratching depth. The results

of the laser belt grinding temperature field inspection also verify the temperature trends in the simulation results.

- (2) Compared with the experimental results of CS, the grinding force of PPLAS decreases with the increase of laser power, and when the laser power is 7.2 W, the grinding force decreases most, at least 60%. The material removal degree becomes higher during PPLAS within a certain range of laser power. Excessive laser power not only reduces the grinding force but also weakens the material removal degree.
- (3) The removal behavior of both CS and PPLAS is plastic removal, and there are tough nests and material tearing features in the chip-substrate sep-

aration zone. The debris of CS has a stacked flake shape with a “fish scale” surface, while it has a fractured and serrated shape during PPLAS. Moreover, the results of the energy spectrum analysis show that there is less damage to the unscratched area during PPLAS.

- (4) The measured and simulated results of PPLAS show that this method can reduce grinding force, increase grinding temperature and improve surface quality. It has potential applications in high-quality and low-damage machining of difficult-to-machine materials such as titanium alloys.

Acknowledgements

Not applicable.

Author Contributions

GX was in charge of the whole research and modified the manuscript; SZ wrote the manuscript, carried out simulations and experiments; YH modified the manuscript; GL and YN modified the manuscript and assisted with the experiments. All authors read and approved the final manuscript.

Authors' Information

Guijian Xiao, born in 1986, is currently an associate professor and a PhD candidate supervisor at *College of Mechanical and Vehicle Engineering, Chongqing University, China*. His main research interests include laser-assisted grinding, materials removal mechanism and belt grinding.

Shengwang Zhu, born in 1998, is currently a master candidate at *College of Mechanical and Vehicle Engineering, Chongqing University, China*.

Yi He, born in 1995, is currently a PhD candidate at *College of Mechanical and Vehicle Engineering, Chongqing University, China*.

Gang Liu, born in 1994, is currently a master candidate at *College of Mechanical and Vehicle Engineering, Chongqing University, China*.

Yuanhe Ni, born in 1999, is currently a master candidate at *College of Mechanical and Vehicle Engineering, Chongqing University, China*.

Funding

Supported by National Natural Science Foundation of China (Grant No. 52175377), Chongqing Municipal Science Foundation (Grant No. CSTB2022N-SCQ-LZX0080), Fundamental Research Funds for Central Universities (Grant Nos. 2023CDJXY-026 and 2023CDJXY-021), National Science and Technology Major Project (Grant No. 2017-VII-0002-0095).

Availability of Data and Materials

The datasets used or analyzed during the current study are available from the corresponding author on reasonable request.

Declarations

Competing Interests

The authors declare no competing financial interests.

Received: 22 October 2022 Revised: 22 August 2023 Accepted: 24 August 2023

Published online: 16 October 2023

References

- [1] B Wang, Z Q Liu, Y K Cai, et al. Advancements in material removal mechanism and surface integrity of high speed metal cutting: A review. *International Journal of Machine Tools and Manufacture*, 2021, 166: 103744.
- [2] A K Khalil, W S Yip, S To. Theoretical and experimental investigations of magnetic field assisted ultra-precision machining of titanium alloys. *Journal of Materials Processing Technology*, 2022, 300: 117429.
- [3] O Kalantari, F Jafarian, M M Fallah. Comparative investigation of surface integrity in laser assisted and conventional machining of Ti-6Al-4V alloy. *Journal of Manufacturing Processes*, 2021, 62: 90-98.
- [4] Z R Liao, A L Monaca, J Murray, et al. Surface integrity in metal machining - Part I: Fundamentals of surface characteristics and formation mechanisms. *International Journal of Machine Tools and Manufacture*, 2021, 162: 103687.
- [5] M H Du, Z Cheng, S S Wang. Finite element modeling of friction at the tool-chip-workpiece interface in high speed machining of Ti6Al4V. *International Journal of Mechanical Sciences*, 2019, 163: 105100.
- [6] R Lindvall, F Lenrick, R M'Saoubi, et al. Performance and wear mechanisms of uncoated cemented carbide cutting tools in Ti6Al4V machining. *Wear*, 2021, 477: 203824.
- [7] Y Hong, S C Xiu, C Sun, et al. Metallographic method for temperature measurement: Reconstruction of grinding temperature field based on critical austenitizing depth and cyclic feedback algorithm. *Journal of Materials Processing Technology*, 2022, 310: 117770.
- [8] G Q Ren, H W Song, J Q Dan, et al. Thermal analysis and machinability for laser-assisted machining of fused silica. *International Journal of Heat and Mass Transfer*, 2020, 148: 119078.
- [9] K Y You, F Z Fang, G P Yan. Surface generation of tungsten carbide in laser-assisted diamond turning. *International Journal of Machine Tools and Manufacture*, 2021, 168: 103770.
- [10] K Y You, G P Yan, X C Luo, et al. Advances in laser assisted machining of hard and brittle materials. *Journal of Manufacturing Processes*, 2020, 58: 677-692.
- [11] C Sun, S C Xiu, Y Hong, et al. Prediction on residual stress with mechanical-thermal and transformation coupled in DGH. *International Journal of Mechanical Sciences*, 2020, 179: 105629.
- [12] Y Cao, W F Ding, B Zhao, et al. Effect of intermittent cutting behavior on the ultrasonic vibration-assisted grinding performance of Inconel718 nickel-based superalloy. *Precision Engineering*, 2022, 78: 248-260.
- [13] K Zhou, J Y Xu, G J Xiao, et al. A novel low-damage and low-abrasive wear processing method of Cf/SiC ceramic matrix composites: Laser-induced ablation-assisted grinding. *Journal of Materials Processing Technology*, 2022, 302: 117503.
- [14] Y Cao, J F Yin, W F Ding, et al. Alumina abrasive wheel wear in ultrasonic vibration-assisted creep-feed grinding of Inconel 718 nickel-based superalloy. *Journal of Materials Processing Technology*, 2021, 297: 117241.
- [15] X Chen, C L Liu, J Y Ke, et al. Subsurface damage and phase transformation in laser-assisted nanometric cutting of single crystal silicon. *Materials & Design*, 2020, 190: 108524.
- [16] Y J Guo, X J Yang, J Kang, et al. Experimental investigations on the laser-assisted machining of single crystal Si for optimal machining. *Optics & Laser Technology*, 2021, 141: 107113.
- [17] Y Ayed, G Germain, W B Salem, et al. Experimental and numerical study of laser-assisted machining of Ti6Al4V titanium alloy. *Finite Elements in Analysis and Design*, 2014, 92: 72-79.
- [18] C R Dandekar, Y C Shin, J Barnes. Machinability improvement of titanium alloy (Ti-6Al-4V) via LAM and hybrid machining. *International Journal of Machine Tools and Manufacture*, 2010, 50(2): 174-182.
- [19] H J Xia, G L Zhao, L Li, et al. Fabrication of high aspect ratio microgroove on Ti6Al4V by laser-induced oxidation assisted micro milling. *Journal of Manufacturing Processes*, 2019, 45: 419-428.
- [20] S A Tadavani, R S Razavi, R Vafaei. Pulsed laser-assisted machining of Inconel 718 superalloy. *Optics & Laser Technology*, 2017, 87: 72-78.
- [21] G Germain, P D Santo, J L Lebrun. Comprehension of chip formation in laser assisted machining. *International Journal of Machine Tools and Manufacture*, 2011, 51(3): 230-238.
- [22] J H Yang, S J Sun, M Brandt, et al. Experimental investigation and 3D finite element prediction of the heat affected zone during laser assisted machining of Ti6Al4V alloy. *Journal of Materials Processing Technology*, 2010, 210(15): 2215-2222.
- [23] Y Xi, H Y Zhan, R A R Rashid, et al. Numerical modeling of laser assisted machining of a beta titanium alloy. *Computational Materials Science*, 2014, 92: 149-156.

- [24] F A Khatir, M H Sadeghi, S Akar. Investigation of surface integrity in laser-assisted turning of AISI 4340 hardened steel: Finite element simulation with experimental verification. *Optics & Laser Technology*, 2022, 147: 107623.
- [25] W F Ding, B Zhao, Q L Zhang, et al. Fabrication and wear characteristics of open-porous cBN abrasive wheels in grinding of Ti-6Al-4V alloys. *Wear*, 2021, 477: 203786.
- [26] L Q Tu, Y D Deng, T C Zheng, et al. Wear and friction analysis of cubic boron nitride tools with different binders in high-speed turning of nickel-based superalloys. *Tribology International*, 2022, 173: 107659.
- [27] Z X Wang, T B Yu, X Z Wang, et al. Grinding temperature field prediction by meshless finite block method with double infinite element. *International Journal of Mechanical Sciences*, 2019, 153-154: 131-142.
- [28] F H Wu, Z J Liu, B S Guo, et al. Research on the burr-free interrupted cutting model of metals. *Journal of Materials Processing Technology*, 2021, 295: 117190.
- [29] M L Wang, N S Qu. Investigation on material removal mechanism in mechano-electrochemical milling of TC4 titanium alloy. *Journal of Materials Processing Technology*, 2021, 295: 117206.
- [30] X Xu, J Zhang, J Outeiro, et al. Multiscale simulation of grain refinement induced by dynamic recrystallization of Ti6Al4V alloy during high speed machining. *Journal of Materials Processing Technology*, 2020, 286: 116834.
- [31] A H Li, J M Pang, J Zhao, et al. FEM-simulation of machining induced surface plastic deformation and microstructural texture evolution of Ti-6Al-4V alloy. *International Journal of Mechanical Sciences*, 2017, 123: 214-223.
- [32] W X Wang, F Salvatore, J Rech, et al. Comprehensive investigation on mechanisms of dry belt grinding on AISI52100 hardened steel. *Tribology International*, 2018, 121: 310-320.
- [33] Z He, J Y Li, Y M Liu, et al. Single-grain cutting based modeling of abrasive belt wear in cylindrical grinding. *Friction*, 2019, 8(1): 208-220.
- [34] Z L Ma, Q H Wang, H Chen, et al. A grinding force predictive model and experimental validation for the laser-assisted grinding (LAG) process of zirconia ceramic. *Journal of Materials Processing Technology*, 2022, 302: 117492.
- [35] X H Zhang, J Jiang, S Li, et al. Laser textured Ti-6Al-4V surfaces and grinding performance evaluation using CBN grinding wheels. *Optics & Laser Technology*, 2019, 109: 389-400.
- [36] K Hokkirigawa, K Kato, Z Z Li. The effect of hardness on the transition of the abrasive wear mechanism of steels. *Wear*, 1988, 123(2): 241-251.
- [37] D de Oliveira, M C Gomes, G V de Oliveira, et al. Experimental and computational contribution to chip geometry evaluation when micromilling Inconel 718. *Wear*, 2021, 476: 203658.
- [38] K Zhou, G J Xiao, J Y Xu, et al. Wear evolution of electroplated diamond abrasive belt and corresponding surface integrity of Inconel 718 during grinding. *Tribology International*, 2023, 177: 107972.
- [39] B X Wei, J Xu, L Q Gao, et al. Nanosecond pulsed laser-assisted modified copper surface structure: Enhanced surface microhardness and microbial corrosion resistance. *Journal of Materials Science & Technology*, 2022, 107: 111-123.
- [40] J Wawrzyniak, J Karczewski, P Kupracz, et al. Laser-assisted modification of titanium dioxide nanotubes in a tilted mode as surface modification and patterning strategy. *Applied Surface Science*, 2020, 508: 145143.
- [41] L Liang, L He, Z K Jiang, et al. Experimental study on the direct planar metallization on glass by the particle sputtering in laser-induced plasma-assisted ablation. *Journal of Manufacturing Processes*, 2022, 75: 573-583.
- [42] A Sassmannshausen, A Brenner, J Finger. Ultrashort pulse laser polishing by continuous surface melting. *Journal of Materials Processing Technology*, 2021, 293: 117058.

Submit your manuscript to a SpringerOpen[®] journal and benefit from:

- Convenient online submission
- Rigorous peer review
- Open access: articles freely available online
- High visibility within the field
- Retaining the copyright to your article

Submit your next manuscript at ► [springeropen.com](https://www.springeropen.com)
